



Cite this: *Nanoscale*, 2017, **9**, 6595

Temperature-dependent optoelectronic properties of quasi-2D colloidal cadmium selenide nanoplatelets†

Sumanta Bose,^{a,b} Sushant Shendre,^{a,c} Zhigang Song,^{a,d} Vijay Kumar Sharma,^{a,c,e,f} Dao Hua Zhang,^{a,b,c} Cuong Dang,^{*a,c} Weijun Fan^{*a,b} and Hilmi Volkan Demir^{*a,c,e,f}

Colloidal cadmium selenide (CdSe) nanoplatelets (NPLs) are a recently developed class of efficient luminescent nanomaterials suitable for optoelectronic device applications. A change in temperature greatly affects their electronic bandstructure and luminescence properties. It is important to understand how and why the characteristics of NPLs are influenced, particularly at elevated temperatures, where both reversible and irreversible quenching processes come into the picture. Here we present a study of the effect of elevated temperatures on the characteristics of colloidal CdSe NPLs. We used an effective-mass envelope function theory based 8-band $k\cdot p$ model and density-matrix theory considering exciton–phonon interaction. We observed the photoluminescence (PL) spectra at various temperatures for their photon emission energy, PL linewidth and intensity by considering the exciton–phonon interaction with both acoustic and optical phonons using Bose–Einstein statistical factors. With a rise in temperature we observed a fall in the transition energy (emission redshift), matrix element, Fermi factor and quasi Fermi separation, with a reduction in intraband state gaps and increased interband coupling. Also, there was a fall in the PL intensity, along with spectral broadening due to an intraband scattering effect. The predicted transition energy values and simulated PL spectra at varying temperatures exhibit appreciable consistency with the experimental results. Our findings have important implications for the application of NPLs in optoelectronic devices, such as NPL lasers and LEDs, operating much above room temperature.

Received 7th January 2017.

Accepted 12th April 2017

DOI: 10.1039/c7nr00163k

rsc.li/nanoscale

1 Introduction

Semiconductor nanoplatelets (NPLs) are a class of atomically flat quasi two-dimensional (2D) quantum confined nanocrystals,

often synthesized using wide bandgap II–VI materials.^{1–4} Advancements in colloidal chemistry have led to the synthesis of high quality single crystal NPL samples.^{1,2} This is assisted by the saturation of dangling bonds on the surface, as the organic ligands block further growth.⁵ This reduces nonradiative recombination paths, enhancing their optical properties. They have attracted increasing interest as they can act as cost-effective and efficient luminophores in display devices, LEDs and lasers.³ They are excellent candidates for such applications owing to their morphological bandgap tunability, fast fluorescence lifetime and unique optical characteristics supporting bright and tunable spectral emission with narrow full-width-at-half-maxima (FWHM) spanning the entire visible to near IR spectral range.^{3,4} They exhibit strong 1D confinement as their thickness is very small (typically a few monolayers (MLs)) compared with the Bohr radius.⁶ Also, they have smaller fluorescent lifetimes than typical colloidal quantum dots (QDs) as a result of fast band-edge exciton recombination. NPLs have been routinely synthesized with a high quantum efficiency of about 50%.⁷ Compared with QDs, they typically have narrower emission spectra, reduced inhomogeneous broadening and sup-

^aSchool of Electrical and Electronic Engineering, Nanyang Technological University, 50 Nanyang Avenue, Singapore 639798, Singapore. E-mail: hcdang@ntu.edu.sg, ewjfan@ntu.edu.sg, hvdemir@ntu.edu.sg

^bOPTIMUS, Centre for OptoElectronics and Biophotonics, Nanyang Technological University, 50 Nanyang Avenue, Singapore 639798, Singapore

^cLUMINOUS! Centre of Excellence for Semiconductor Lighting & Displays and TPI – The Photonics Institute, Nanyang Technological University, Singapore 639798, Singapore

^dState Key Laboratory of Superlattices and Microstructures, Institute of Semiconductors, Chinese Academy of Sciences, Beijing 100083, People's Republic of China

^eSchool of Physical and Mathematical Sciences, Nanyang Technological University, 50 Nanyang Avenue, Singapore 639798, Singapore

^fDepartment of Physics, Department of Electrical and Electronics Engineering and UNAM, Institute of Materials Science and Nanotechnology, Bilkent University, Turkey

†Electronic supplementary information (ESI) available: TE/TM mode TMEs, NPLs dimension analysis, quasi-Fermi energy levels, Fermi factor, intraband state gaps, results comparison and validation, TRPL fit & response, and comparative (experiment and theory) data tables. See DOI: 10.1039/C7NR00163K

pressed Auger recombination. Recently, for the first time, continuous wave laser operation has been demonstrated using colloidal NPLs.⁸

With the recent developments and potential applications of NPLs in commercial optoelectronic devices,^{7,8} it is imperative to study their characteristics and performance at elevated temperatures – when both reversible and irreversible luminescence quenching processes come into play.⁹ In this work, we study in tandem, using theoretical modeling and experimental measurements, the underlying physical phenomena determining the optoelectronic characteristics of CdSe NPLs across varying temperatures above room temperature (RT). Achtstein *et al.*¹⁰ studied NPL characteristics at the cryogenic range, while there are several works studying QDs and other nanocrystals across varying temperature ranges.^{11–13} But, work addressing the study of NPL optoelectronic properties at elevated temperatures above RT has not been reported thus far. We begin by laying down the theoretical framework, followed by a comprehensive discussion on the obtained results to understand the physics of the NPLs at elevated temperatures, and present experimental methods at the end.

2 Theoretical framework

2.1 Electronic bandstructure

Here we study CdSe NPLs in the zinc blende (ZB) phase as they are colloiddally synthesized. The surrounding dielectric medium formed by the ligands in colloidal solutions helps in optical property enhancement by surface electronic state passivation and also in stabilizing them. In our model we construct each NPL atom-by-atom in a 3D structure and use an effective mass envelope function theory approach based on the 8-band $\mathbf{k}\cdot\mathbf{p}$ method. This is used to solve the eigenvalue equation to obtain the eigenenergy values and electronic structure around the Γ -point of the Brillouin zone. We simultaneously take into account the nonparabolicity of the coupled valence band (VB) and conduction band (CB) including the split-off bands. Using the Bloch function basis of $|s\rangle\uparrow$, $|11\rangle\uparrow$, $|10\rangle\uparrow$, $|1-1\rangle\uparrow$, $|s\rangle\downarrow$, $|11\rangle\downarrow$, $|10\rangle\downarrow$, $|1-1\rangle\downarrow$, the 8-band Hamiltonian can be expressed as¹⁴

$$H_{8\times 8} = \begin{pmatrix} A & \frac{i\hbar\sqrt{E_p}(k_x+ik_y)}{2\sqrt{m_0}} & i\hbar\sqrt{\frac{E_p}{2m_0}}k_z & \frac{i\hbar\sqrt{E_p}(k_x-ik_y)}{2\sqrt{m_0}} & 0 & 0 & 0 & 0 \\ \text{c.c.} & B & C & D & 0 & 0 & 0 & 0 \\ \text{c.c.} & \text{c.c.} & E & C & 0 & 0 & 0 & 0 \\ \text{c.c.} & \text{c.c.} & \text{c.c.} & B & 0 & 0 & 0 & 0 \\ \text{c.c.} & \text{c.c.} & \text{c.c.} & \text{c.c.} & A & \frac{i\hbar\sqrt{E_p}(k_x+ik_y)}{2\sqrt{m_0}} & i\hbar\sqrt{\frac{E_p}{2m_0}}k_z & \frac{i\hbar\sqrt{E_p}(k_x-ik_y)}{2\sqrt{m_0}} \\ \text{c.c.} & \text{c.c.} & \text{c.c.} & \text{c.c.} & \text{c.c.} & B & C & D \\ \text{c.c.} & \text{c.c.} & \text{c.c.} & \text{c.c.} & \text{c.c.} & \text{c.c.} & E & C \\ \text{c.c.} & B \end{pmatrix} + H_{\text{so}} + V_{\text{NPL}} \quad (1)$$

where all the quadratic, linear and independent terms of k are in the first Hamiltonian matrix, with $H_{ij} = H_{ji}^*$, denoted by c.c. standing for the complex conjugate. E_p is the Kane's theory matrix element and V_{NPL} is the NPL confining potential. The

expressions for the Hamiltonian elements of eqn (1), A through E are detailed below. The modified wavevectors, k'_x, k'_y, k'_z are calculated using the 3×3 strain tensor matrix, ε :

$$A = -\frac{\hbar^2}{2m_0}\gamma_c(k_x^2 + k_y^2 + k_z^2) + a_c[\text{tr}(\varepsilon)] + E_g \quad (2a)$$

$$B = -\frac{\hbar^2}{2m_0}\left[\frac{L'+M'}{2}(k_x^2 + k_y^2) + M'k_z^2\right] + a_v[\text{tr}(\varepsilon)] + \frac{b}{2}[\text{tr}(\varepsilon) - 2\varepsilon_{zz}] \quad (2b)$$

$$C = -\frac{\hbar^2}{2m_0}\left[\frac{N'(k_x - ik_y)k_z}{\sqrt{2}}\right] + \sqrt{6}d(\varepsilon_{xz} - i\varepsilon_{yz}) \quad (2c)$$

$$D = -\frac{\hbar^2}{2m_0}\left[\frac{L'-M'}{2}(k_x^2 - k_y^2) - iN'k_xk_y\right] - i\sqrt{12}d\varepsilon_{xy} + \frac{3b}{2}(\varepsilon_{xx} - \varepsilon_{yy}) \quad (2d)$$

$$E = -\frac{\hbar^2}{2m_0}\left[M'(k_x^2 + k_y^2) + L'k_z^2\right] + a_v[\text{tr}(\varepsilon)] + b[3\varepsilon_{zz} - \text{tr}(\varepsilon)] \quad (2e)$$

$$\gamma_c = -\frac{E_p}{3}\left[\frac{1}{E_g + \Delta_{\text{so}}} + \frac{2}{E_g}\right] + \frac{m_0}{m_e^*} \quad (2f)$$

$$\begin{pmatrix} k'_x \\ k'_y \\ k'_z \end{pmatrix} = (I_3 - \varepsilon) \begin{pmatrix} k_x \\ k_y \\ k_z \end{pmatrix} \quad (2g)$$

Using the Luttinger–Kohn effective mass parameters $\gamma_1, \gamma_2, \gamma_3$ as listed in Table 1, we have derived the modified Luttinger parameters for our calculation:

$$L' = L - \frac{E_p}{E_g} = -\frac{\hbar^2}{2m_0}(\gamma_1 + 4\gamma_2 + 1) \quad (3a)$$

$$M' = M = -\frac{\hbar^2}{2m_0}(\gamma_1 - 2\gamma_2 + 1) \quad (3b)$$

$$N' = N - \frac{E_p}{E_g} = -\frac{\hbar^2}{2m_0}(6\gamma_3) \quad (3c)$$

Table 1 Physical material parameters of CdSe at room temperature

Symbol (unit)	Physical parameter	Value ^{ref.}
E_g (eV)	Bandgap energy	1.732 ^a
E_p (eV)	Kane matrix element	16.5 ^a
Δ_{so} (eV)	Spin-orbit splitting energy	0.42 ^b
γ_1	Luttinger-Kohn parameters	3.265 ^c
γ_2		1.162 ^c
γ_3		1.443 ^c
m_e^*/m_0	Effective electron mass	0.12 ^d
m_h^*/m_0	Effective hole mass	0.45 ^d
a_c (eV)	Hydrostatic deformation potential of CB	-2.83 ^a
a_v (eV)	Hydrostatic deformation potential of VB	1.15 ^a
b (eV)	Sheer deformation potential	-1.05 ^a
d (eV)	Sheer deformation potential	-3.10 ^a
a_0 (Å)	Lattice constant	6.052 ^d
d_0 (Å)	Interatomic bond-length	2.620 ^e
α (N m ⁻¹)	Bond-stretching force constant	35.22 ^e
β (N m ⁻¹)	Bond-bending force constant	3.14 ^e
n_r	Refractive index	2.5 ^a
a_B (nm)	Bohr radius	5.6 ^f

^a Ref. 18. ^b Ref. 19. ^c Ref. 20. ^d Ref. 21. ^e Ref. 22. ^f Ref. 23.

H_{so} , given by eqn (4) is the VB spin-orbit coupling Hamiltonian:

$$H_{so} = \frac{\Delta_{so}}{3} \begin{pmatrix} 0 & 0 & 0 & 0 & 0 & 0 & 0 & 0 \\ 0 & 0 & 0 & 0 & 0 & 0 & 0 & 0 \\ 0 & 0 & -1 & 0 & 0 & -\sqrt{2} & 0 & 0 \\ 0 & 0 & 0 & -2 & 0 & 0 & \sqrt{2} & 0 \\ 0 & 0 & 0 & 0 & 0 & 0 & 0 & 0 \\ 0 & 0 & -\sqrt{2} & 0 & 0 & -2 & 0 & 0 \\ 0 & 0 & 0 & \sqrt{2} & 0 & 0 & -1 & 0 \\ 0 & 0 & 0 & 0 & 0 & 0 & 0 & 0 \end{pmatrix} \quad (4)$$

Considering the NPL periodicities to be L_x , L_y , L_z along the x , y and z directions, we use plane waves to expand the eight-dimensional hole and electron envelope wave function as¹⁵

$$\phi_m = \{\phi_m^j\} \quad (j = 1, 2, \dots, 8) \quad (5a)$$

with

$$\phi_m^j = \frac{1}{\sqrt{V}} \sum_{n_x, n_y, n_z} a_{m, n_x, n_y, n_z}^j e^{i(k_{nx}x + k_{ny}y + k_{nz}z)} \quad (5b)$$

where $k_{nx} = 2\pi n_x/L_x$, $k_{ny} = 2\pi n_y/L_y$, $k_{nz} = 2\pi n_z/L_z$ and n_x , n_y , n_z are the plane wave numbers. And $V = L_x L_y L_z$. The indices of the basis and energy subbands are given by j and m respectively.

Now, the interatomic interactions in the NPL cause atomistic relaxations which can be estimated by employing the microscopic theory of a valence force field (VFF) model, wherein we account for 2-body interaction (atomic-bond-stretching) and 3-body interaction (atomic-bond-bending). The sum total of the strain energy is given by¹⁶

$$E_{VFF} = \sum_{i(j)} \frac{3\alpha_{ij}}{16d_{0,ij}^2} (|\mathbf{r}_i - \mathbf{r}_j|^2 - d_{0,ij}^2)^2 + \sum_{i(j,k)} \frac{3\beta_{jik}}{8d_{0,ij}d_{0,ik}} (|\mathbf{r}_i - \mathbf{r}_j||\mathbf{r}_i - \mathbf{r}_k| - \cos \hat{\theta}_{ijk} d_{0,ij}d_{0,ik})^2 \quad (6)$$

where the atoms in the crystal lattice are identified by the indices i, j and k . $d_{0,ij}$ is the ideal atomic bond-length between the i^{th} and j^{th} atoms, with $4d_{0,ij} = \sqrt{3}a_{0,ij}$ relating it to $a_{0,ij}$, the lattice constant.¹⁷ Factors such as external piezoelectric strain or temperature cause deviations in the bond-length from the ideal $d_{0,ij}$, and the bond-distance between the i^{th} and j^{th} atoms in the system studied is given by $|\mathbf{r}_i - \mathbf{r}_j|$, where \mathbf{r}_i is the position vector of the i^{th} atom. The bond-stretching force constant of the i - j bond is given by α_{ij} (Table 1). The ideal bond-angle of the bond among the i^{th} , j^{th} and k^{th} atoms (vertexed at i^{th} atom) is given by $\hat{\theta}_{ijk}$ ($= 1/3$ for ZB structures). The bond-bending force constant of the j - i - k bond-angle is given by β_{jik} (Table 1).

2.2 Optical properties

For studying the optical characteristics of NPLs, we use the density-matrix equation dependent on the quasi Fermi levels of the CB (f_c) and VB (f_v). We can estimate it for a two-dimensional structure with exciton effects as a sum of the spontaneous radiative rate from the excitonic bound states, $r_{sp}^{\text{ex,b}}$ and continuum-states, r_{sp}^c . The excitonic bound state contribution is given by^{24,25}

$$r_{sp}^{\text{ex,b}}(E) = \frac{e^2 n_r E}{\pi m_0^2 \epsilon_0 c^3 \hbar^2 t} \sum_{c,v} |\Psi_{1s}^{\text{cv}}(0)|^2 |\mathcal{I}_{cv}^2| |I_{cv}|^2 \times f_c(1 - f_v) \mathcal{I}(E - E_{cv} - E_b) \quad (7a)$$

$$\Psi_{1s}(x) = \frac{4\beta}{a_B \sqrt{2\pi}} e^{-2x\beta/a_B} \quad (7b)$$

$$E_b = -4\beta^2 R_y \quad (7c)$$

where the symbols (e , n_r , E , m_0 , ϵ_0 , c , \hbar) have standard physical meanings. t is the NPL thickness, $\Psi_{1s}(x)$ is the 1s exciton envelope function and x is the relative distance between the electron and hole along the transverse direction in the NPL. f_c and f_v are the Fermi-Dirac distributions of the CB and VB, dependent on the quasi-Fermi energy levels of the CB (E_{fc}) and VB (E_{fv}), respectively. $I_{cv} = \int \Psi^{E(c)}(z) \Psi^{H(v)}(z) dz$ is the overlap integral between the electron and hole wavefunctions along the transverse direction. E_b is the 1s exciton binding energy and β is a variational parameter, taken to be 1 for two-dimensional structures, based on the conclusive observation that for two-dimensional semiconductors, the binding energy increment by the low dielectric constant of the surface ligands and the solvent is almost exactly compensated by the self-interactions of electrons and holes with self-image potential.⁴ $a_B = 4\pi\epsilon_0\epsilon_r\hbar^2/m_r e^2$ and $R_y = m_r e^4/32\pi^2\epsilon_0^2\epsilon_r^2\hbar^2$ are the excitonic Bohr radius and excitonic Rydberg energy respectively, where m_r is the reduced mass of the electron-hole pair: $m_r^{-1} = m_e^{-1} + m_h^{-1}$ and ϵ_r is the relative permittivity. For the continuum state contributions, we have^{25,26}

$$r_{sp}^c(E) = \frac{e^2 n_r E}{\pi m_0^2 \epsilon_0 c^3 \hbar^2 V} \sum_{c,v} |\mathcal{I}_{cv}|^2 f_c(1 - f_v) \times S_{2D}(E - E_{cv}) \mathcal{I}(E - E_{cv}) \quad (8a)$$

$$S_{2D}(E - E_{cv}) = \frac{2}{1 + \exp(-2\pi\sqrt{R_y}/(E - E_{cv}))} \quad (8b)$$

where $S_{2D}(E)$ is the 2D Sommerfeld enhancement factor.²⁶ V is the NPL volume in real space. The PL emission is the maximum when $f_c = 1$ (fully occupied upper level) and $f_v = 0$ (fully empty lower level), and the emission rate is $\propto f_c(1 - f_v)$, which is called the Fermi factor.²⁷ The calculation of the theoretical PL also takes into consideration the spectral transition energy broadening (dephasing) effect accounted for by the Lorentzian broadening lineshape term $\mathcal{S}_{cv}(E - E_{cv})$ in eqn (7a) and (8a), given by

$$\mathcal{S}_{cv}(E - E_{cv}) = \frac{1}{\pi} \frac{\hbar/\tau_{in}}{(E - E_{cv})^2 + (\hbar/\tau_{in})^2} \quad (9)$$

whose full width at half maximum (FWHM) is $2\hbar/\tau_{in}$ and scattering probability per unit time is $1/\tau_{in}$, where τ_{in} is the intra-band relaxation time. The term $|\mathcal{S}_{cv}|^2$ in eqn (7a) and (8a) is the square of the optical transition matrix element (TME). It quantifies the strength of transition between the electron- and hole-subband.²⁸ We calculate it using the momentum operator, \mathbf{p} and the real electron and hole wavefunctions, $\Psi_{c,k}$ and $\Psi_{v,k}$ respectively: $\mathcal{S}_{cv,i} = \langle \Psi_{c,k} | \hat{e}_i \cdot \mathbf{p} | \Psi_{v,k} \rangle$, $i = x, y, z$.²⁹ Expressions for $\mathcal{S}_{cv,i}$ along the x , y and z directions are given in the ESI.† The average of $\mathcal{S}_{cv,x}$ and $\mathcal{S}_{cv,y}$ (TMEs along x and y directions) contributes to the transverse electric (TE) mode emission, while $\mathcal{S}_{cv,z}$, the TME along the z direction contributes to the transverse magnetic (TM) mode emission. The TE mode emission is x - y plane polarized, while the TM mode emission is z direction polarized. Table 1 lists the material parameters of CdSe used in this work, citing their sources. Now, in section 3, using this theoretical framework, we study the effect of temperature on the optoelectronic properties of CdSe NPLs and compare it with the experimental results.

3 Results and discussion

3.1 Theoretical results

We have used the theoretical model described in section 2 to study the optoelectronic characteristics of quasi two-dimensional colloidal CdSe NPLs of lateral dimensions of $22 \text{ nm} \times 8 \text{ nm}$, and a vertical thickness of 4 monolayer (ML), across temperatures varying from room temperature (RT) to 90°C . We have modeled and studied NPLs of these particular dimensions, based on experimental measurements as we shall describe later in section 3.2. Under this scheme, we have studied how temperature affects their electronic structure and optical properties and predicted some temperature-dependent photoluminescence (PL) characteristics of CdSe NPLs. Fig. 1a shows the theoretically calculated excitonic transition energy (and photon emission wavelength) from the bottom of CB (E1) to the top of VB (H1) *i.e.* E1–H1, as a function of temperature. With an increase in temperature there is a red shift in the transition energy (photon emission energy). The reason is that the bandgap, E_g has a negative thermal coefficient (dE_g/dT) due to

(i) lattice thermal dilatation and electron–phonon interaction $\propto T$ at high temperatures, and (ii) electron–phonon interaction $\propto T^2$ at low temperatures. In this context, we conventionally have the Varshni relation³⁰ to explicate the behavior of E_g . However, detailed systematic studies for II–VI semiconductors have shown that sometimes the Varshni relation may not be very accurate.³¹ Another semiempirical expression suggested by Cardona *et al.*³² is more accurate as we shall subsequently see. Also, with an increase in temperature, the phonon concentration increases and causes increased scattering and non-radiative recombinations start occurring,³³ which causes the E1–H1 TME to decrease.

Of the eight temperature cases studied in Fig. 1a, we present the electronic bandstructure and the probability of band mixing between conduction electrons and valence heavy-, light- and split-off-holes due to coupling for the 4 ML CdSe NPLs at 30, 50 and 70°C , in Fig. 1b–d. The E states represent

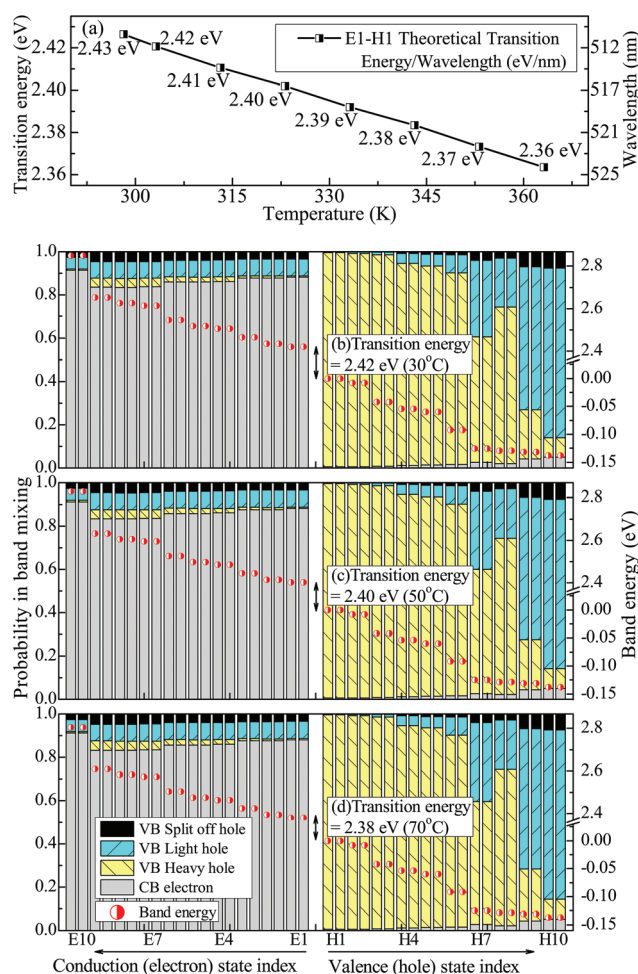


Fig. 1 (a) Theoretical E1–H1 (bottom of conduction band to top of valence band) excitonic transition energy/wavelength as a function of temperature. Frames (b–d) show the electronic bandstructure and the probability in band mixing between conduction electrons and valence heavy-, light- and split off holes for 4 ML CdSe NPLs at (b) 30°C , (c) 50°C and (d) 70°C . E1–H1 transition energies are indicated. Legends show the band mixing probabilities.

the conduction electron states, while the H states represent the valence hole states. Each of the states is two-fold degenerate, considering spin-up and spin-down alternatives. For the sake of discussion, let us consider the 4 ML CdSe NPL at 30 °C of Fig. 1a as a case. The E1–H1 transition energy (2.42 eV) determines the PL peak emission energy.[‡] The CB states mainly comprise electrons with a very low composition of *hh*, *lh* and split-off (*so*) hole, which comes from the coupling effects. The effective *hh* mass is much larger than the effective electron mass for CdSe,²¹ thus the *hh* dispersion curve is flatter than the conduction dispersion curve. Therefore, the first ten hole levels span only ~140 meV, while the first ten electron levels span ~425 meV. In the VB, the first few levels are *hh* dominated followed by an increased influence of *lh* and *so*. Comparing the span of the first ten electron and hole states and band-mixing probabilities of the three cases in Fig. 1 we have two significant observations: (i) an increase in temperature induces a faster reduction in the intra-CB state gaps compared with the intra-VB state gaps. For instance, for a temperature rise of 20 °C between the adjacent frames of Fig. 1, the Δ_{E1-H10} is over five times larger than the Δ_{H1-H10} . This is by virtue of the temperature-induced thermal lattice dilatation effects, given that the deformation potential of the CB is higher than that of the VB for CdSe; and (ii) an increase in temperature promotes e–h quantum state coupling – the conduction states start to have an increased contribution from holes and *vice versa*. Moreover, the intraband dynamics is also affected, such that the role of the dominant contributor diminishes with increasing temperature. For instance, the dominant contributors for H1 through H8 is *hh* while for H9 and H10 is *lh*, whose contribution falls as temperature rises. The contrast is, however, too small to be reflected graphically. These band-mixing probabilities are affected by the varying degrees of coupling between the conduction electrons and valence *hh*, *lh* and *so* holes, which can be empirically determined. For each level, the band-mixing probabilities are dictated by their aggregate electron and hole wavefunctions and the associated charge densities thereof.

The Fermi factor and energy levels are important determiners of the temperature-dependent optoelectronics characteristics. In Fig. 2a we show the Fermi factor $f_c(1 - f_v)$ at E1–H1 transition and in Fig. 2b the Fermi energy separation $\Delta F = E_{fc} - E_{fv}$ in our 4 ML CdSe NPL as a function of temperature, for varying photogenerated carrier densities from 1 to $5 \times 10^{19} \text{ cm}^{-3}$. The ΔF for each case is compared with the E1–H1 transition energy, and $\Delta F > \text{E1-H1}$ ensures the Bernard–Duraffourg inversion condition (population inversion) necessary for lasing.²⁶ With an increase in carrier density, both Fermi factor and Fermi energy separation increase. However, as we continue to increase the density, the extent of Fermi factor increment falls, as it approaches saturation. However, a

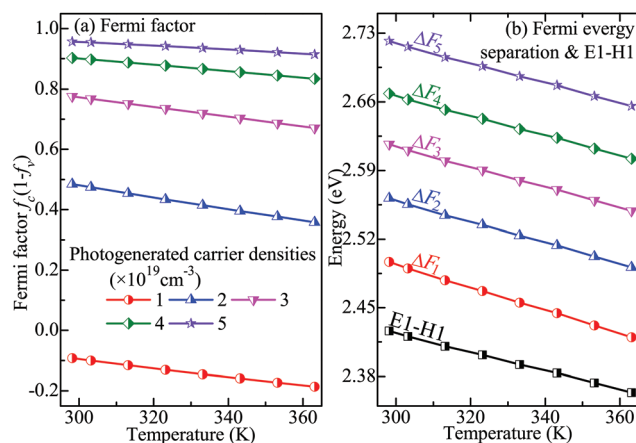


Fig. 2 (a) Fermi factor $f_c(1 - f_v)$ for E1–H1 transition, and (b) Fermi energy separation $\Delta F = E_{fc} - E_{fv}$ compared with the E1–H1 transition energy in 4 ML CdSe NPLs as a function of temperature for varying injection carrier concentration. Both, Fermi factor and ΔF have a negative temperature gradient.

rise in temperature has detrimental effects on both Fermi factor and Fermi energy separation. With an increase in temperature, the fermions (electrons and holes) become thermally excited and therefore the probability of occupying higher CB and VB energy states is increased; so the f_c falls, while f_v rises. Consequently the Fermi factor decreases with temperature. Also, the quasi Fermi levels of the CB and VB (E_{fc} and E_{fv}) approach the band edges, and ΔF falls. In the ESI,[†] we have shown the E_{fc} and E_{fv} in contour forms along with the Fermi factor and Fermi energy separation.

Another critical temperature-dependent optoelectronic factor is the transition matrix element (TME) which is shown in Fig. 3 for the E1–H1 transition in TE mode as a function of temperature. As the thermally excited fermions begin to occupy higher energy states the E1–H1 transition weakens. A physical equivalent of the TME is the oscillator strength $f_{cv} \propto \mu_{cv}^2$, where μ_{cv} is the transition dipole moment, and it can be calculated from the TME using $\mu_{cv} = e\hbar \mathcal{P}_{cv} / im_0 E_{cv}$. It allows us to quantify the transition strength from state *c* to *v*, which decreases with a rise in temperature.

Now we shall study the spatial manifestation of the electronic states. Fig. 4 shows the spatial charge densities of the

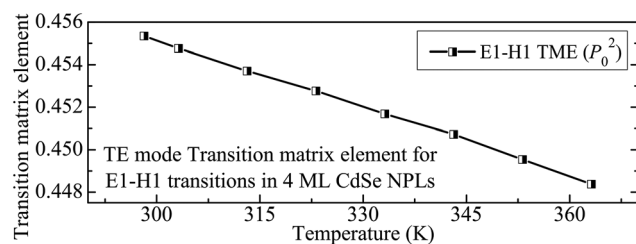


Fig. 3 TE mode transition matrix element (TME) for the E1–H1 transitions as a function of temperature in 4 ML CdSe NPL. The other interband TMEs (both TE and TM mode) are given in the ESI.[†]

[‡] Later in section 3.2 we will show that the experimental PL emission spectrum of 4 ML CdSe NPL at 30 °C (Fig. 6) has its peak emission at 512 nm corresponding to the transition energy of 2.42 eV predicted by our model.

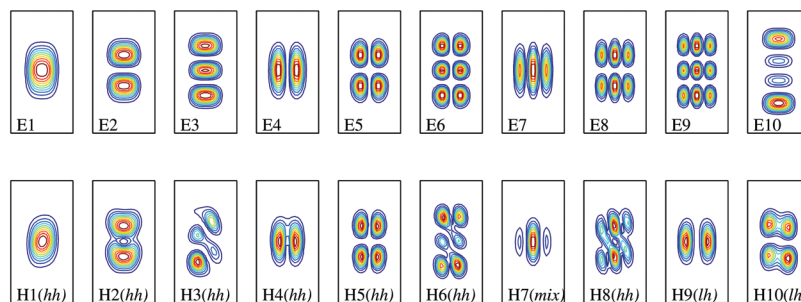


Fig. 4 The spatial charge density of the first ten electron and hole states of 4 ML CdSe NPLs at 30 °C (303.15 K) cut along the vertically central x - y plane ($z = 0$) of the NPL. Warmer (reddish) colors depict higher occupation probability over cooler ones (bluish). The rectangular boundary depicts our studied NPL (22 nm \times 8 nm), but the dimensions are not to scale, for the sake of comprehensive visual representation.

first ten electron and hole states (square of the wavefunction $|\psi^2|$, *i.e.* probability of finding them), within the vertically central x - y plane of the 4 ML CdSe NPL at 30 °C corresponding to Fig. 1b. The charge density description in terms of s and p orbitals is quite a general feature of III-V semiconductors. However in II-VI semiconductors the VB is influenced by chemically active d orbitals also.³⁴ The E1, H1 and H7 states are s -like. While H1 is dominated by hh , H7 has higher lh contribution. The E2 and H2 are p_y -like, while E4, H4 and H9 are p_x -like – H4 has greater hh influence while H9 has more of lh . The E3, E7 and H3 are formed by s - p -mixing. The E5 and H5 are d_{xy} -like, while the E6 and H6 again have some amount of mixing. It is observed that with changes in temperature the spatial charge densities have very inconsequential variations because they are a measure of the electron and hole probability density determined by the wavefunction localization, which is primarily affected by piezoelectric strain and external electric fields.

3.2 Experimental results

We have synthesized 4 monolayer (ML) CdSe NPLs as they have been most widely investigated in the literature^{7,18,35–39} and found applications in LED color-conversion layers, lasers and luminescent solar concentrators. We have used colloidal synthesis techniques similar to those used in ref. 38 and 40–42 as described in the Experimental methods section.

Fig. 5 shows a high-resolution transmission electron microscopy (TEM) image of our synthesized NPL ensemble population. We can observe NPLs in two orientations: face view (laterally flat) and edge view (vertically stacked). We have done lateral dimension measurements over several NPL samples using ImageJ software. Their average length and width were measured to be 22 nm and 8 nm respectively. The theoretical results discussed in section 3.1 correspond to the same dimensions as our synthesized NPLs. Measurements of stacked NPLs reveal differing thicknesses at the two ends, which is attributed to NPL tilting/folding, a common phenomenon for NPLs, was also observed by several other groups.^{4,43} Also, the ligands surrounding the NPLs have a contrast in the TEM image, so the NPL boundary is not strictly discernible. However, the confirmation of 4 ML (1.2 nm) thickness comes

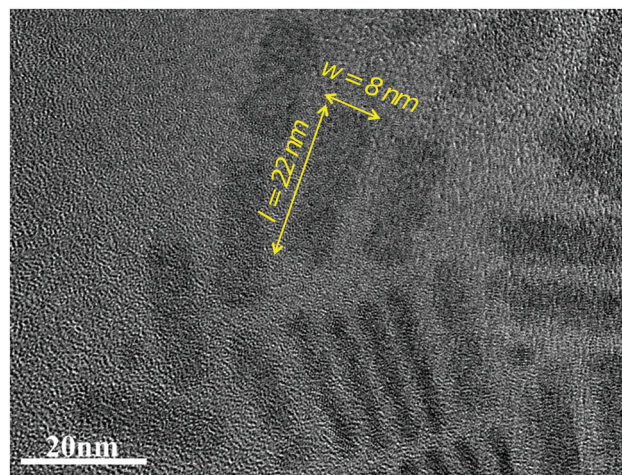


Fig. 5 High-resolution transmission electron microscopy (TEM) image of 4 ML CdSe NPL ensemble population. Average lateral dimension is $l = 22$ nm and $w = 8$ nm (scale: 20 nm).

from the optical spectra characterization. This is discussed in the ESI.†

The spectral characterization results in Fig. 6 show the experimental PL emission and absorption spectrum (both measured in solution form) for our 4 ML CdSe NPLs at 30 °C. The PL was measured by using a standard PL spectrometer with an excitation wavelength of 350 nm. We can observe the PL emission peak at 512 nm, which is in very good agreement with the E1–H1 transition energy prediction of 2.42 eV obtained by our model, as shown in Fig. 1a and b. Similarly, with our E1–H1 predictions at other varying temperatures (Fig. 1a) we can determine their expected PL emission wavelengths.

With a Stokes shift of 3 nm from the PL spectrum, the primary absorption peak occurs at 509 nm. This is due to the reorganization of the solvent in solution-processed NPLs plus the dissipation and vibrational relaxation of the NPLs.⁴⁴ The primary absorption peak corresponds to the E1–H1 transition, where the H1 state is 2D-heavy hole (hh) dominated [as theoretically determined in Fig. 1b]. A study of the TMEs makes this clear. The transverse electric (TE)

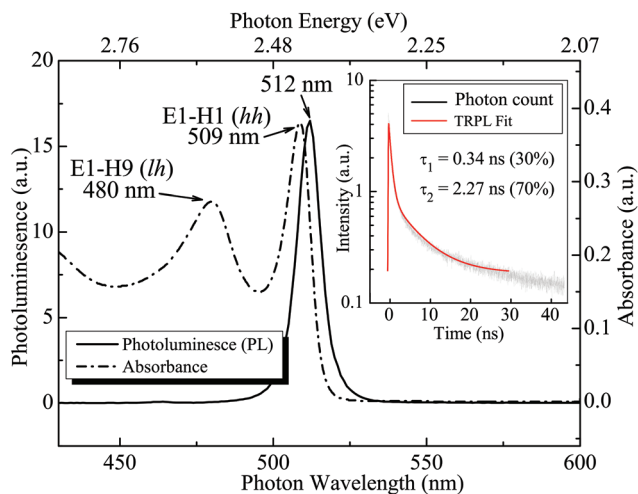


Fig. 6 Experimental photoluminescence (PL) and absorption spectrum of 4 ML CdSe NPLs at 30 °C (303.15 K). The PL excitation wavelength was 350 nm. Both PL and absorption were measured in solution form. PL peak is at 512 nm. Primary absorption peak, at 509 nm has a Stokes shift of 3 nm, while the secondary absorption peak is at 480 nm. Inset shows time-resolved PL (TRPL) spectrum and fit measured in thin-film form at 30 °C. The fit and the system response is given in the ESI.†

mode TME for the E1–H1 transition is maximal among all possible cases, accounting to 0.455. The secondary absorption peak occurs at 480 nm. A study of the transverse magnetic (TM) mode TMEs of the transitions near the secondary absorption energy shows that this comes from E1–H9 transitions, for which the TME value is 0.358, which is weaker than the E1–H1 TME but is stronger than the TMEs of the other allowed transitions. The fraction of light holes (*lh*) involved in this transition is much higher (66%) than their *hh* counterpart (22%) [Fig. 1b]. This conforms with the idea that *hh* contributes to the primary absorption peak of a typical CdSe NPL, while *lh* contributes to the secondary peak.¹⁰ We have discussed the TE and TM mode TME values for all possible transitions between E_{1–10} to H_{1–10} in the

ESI.† Note that the PL peak position at 512 nm and the *hh* and *lh* absorption peaks at 509 nm and 480 nm, respectively, confirm that our synthesized NPL samples are indeed 4 ML (1.2 nm) thick.^{38,45}

The time-resolved PL (TRPL) spectrum and fit at 30 °C (inset of Fig. 6) reveal a dual decay path mechanism following the model $I(t) = a_1e^{-t/\tau_1} + a_2e^{-t/\tau_2}$, with PL decay lifetimes of $\tau_1 = 0.34$ ns and $\tau_2 = 2.27$ ns with 30% and 70% contribution, respectively, leading to an average lifetime of 2.15 ns calculated using $\tau_{\text{avg}} = (a_1\tau_1^2 + a_2\tau_2^2)/(a_1\tau_1 + a_2\tau_2)$, which is similar to a previously reported τ_{avg} of CdSe NPLs at RT.⁴⁶ The TRPL fit is shown again with the system response in the ESI.† Previous radiative transition dynamics studies on CdSe NPLs have also observed a similar dual decay path mechanism where τ_1 is assigned as the radiative recombination decay time period relating to reversible PL losses, while τ_2 is assigned as the nonradiative recombination decay time period relating to the trap states which may cause irreversible losses in the PL intensity^{10,46} originating from the fast hole-trapping due to incomplete passivation of Cd atoms on the NPL surface.⁴⁰

Fig. 7a and b show the effect of temperature on the experimentally measured PL spectra of the NPLs in thin-film form using a laser excitation wavelength of 355 nm at 0.5 mW power, during ascending and descending temperature respectively. For every 10 °C rise in temperature, there is a red-shift in the emission wavelength of ~2 nm, and the PL intensity falls as the sample quality degrades. Also, the spectrum broadens due to the intraband scattering effect. Fig. 8 shows the photon emission energy, PL linewidth and PL integrated intensity as a function of ascending (black □) and descending (red ×) temperature. For a particular temperature the emission energy and linewidth are almost identical in both. While cooling back to RT, the signal intensity increases, but is far from being retraced. The recovery is <14% (see logarithmic comparison in Fig. 8d). The effective photon emission energy (equivalent to the effective E1–H1 transition energy) has a negative thermal coefficient as already discussed in the context of Fig. 1a. For II–VI semiconductors, a semiempirical expression (eqn (10)) suggested by Cardona *et al.*³² takes into consideration the

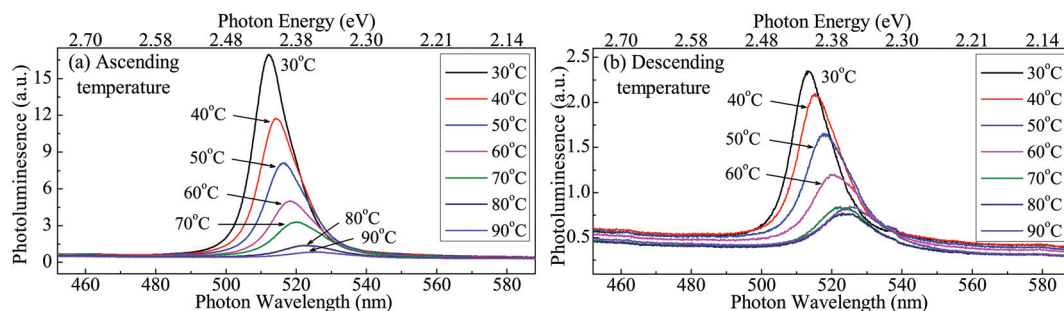


Fig. 7 PL spectra of 4 ML CdSe NPLs measured in thin-film form while (a) ascending, and (b) descending temperature, respectively. Temperature of each PL spectrum is indicated. With an increase in temperature there is a redshift in the emission peak, broadening in the PL linewidth and reduction in PL intensity. Upon decreasing the temperature to RT, we observe substantial retractability in the peak position and linewidth, but not in the intensity. Fig. 8 shows the PL emission energy (peak position), linewidth and integrated intensity as a function of temperature.

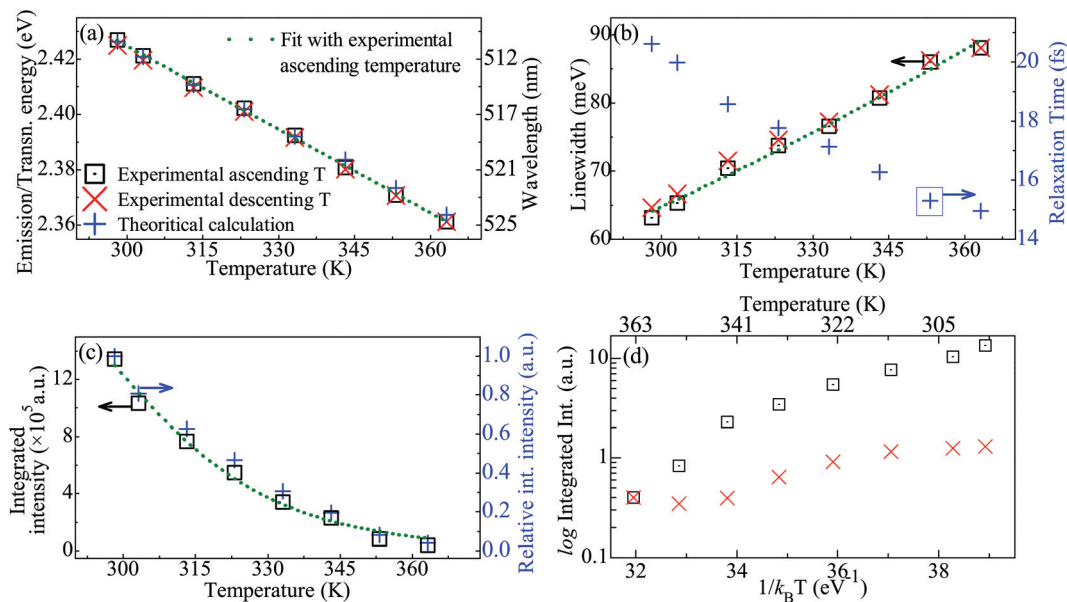


Fig. 8 (a) Experimental PL emission energy/wavelength while ascending and descending temperature compared with theoretically simulated E1–H1 transition energy values. (b) Experimental PL linewidth while ascending and descending temperature and extracted intraband relaxation time τ_{in} used in theoretical model [eqn (9)] from data of ascending temperature. (c) Experimental PL intensity while ascending temperature compared with theoretically simulated relative PL integrated intensity; and (d) comparative Arrhenius plot for PL integrated intensity (log scale) while ascending and descending temperature. Consistent symbols have been used in all the frames: black \square and red \times for experimental data while ascending and descending temperature respectively, while blue $+$ for theoretically predicted data or data used in theoretical model (comparison is discussed in section 3.3). The green dotted lines in frames (a), (b) and (c) show the fitted plots [using eqn (10), (11) and (12)] with the data of ascending temperature.

phonon emission and absorption using Bose–Einstein statistical factors:

$$E_{exc}(T) = E_{exc}(0) - a_{ep}(2n_B + 1) \quad (10)$$

Here a_{ep} is the exciton–phonon coupling constant and $n_B = 1/(e^{\Theta/T} - 1)$. Θ is the average phonon temperature, such that the average phonon energy is $k_B\Theta$. Both acoustic and optical phonons contribute to the redshift incurred by increasing temperature. $E_{exc}(0)$ is the exciton energy at 0 K. T is the absolute temperature. Upon fitting the ascending temperature data of Fig. 8a with eqn (10), we get $E_{exc}(0) = 2.727$ eV. This value is in good agreement with results of Achtstein *et al.*,¹⁰ who reported 2.709 eV. This elevated $E_{exc}(0)$ compared with the bulk-like ZB CdSe epilayers (1.739 eV)⁴⁷ is due to increased quantum confinement effects. Further, we obtain $a_{ep} = 18.2 \pm 2.8$ meV and $\Theta = 36 \pm 0.4$ K. Chia *et al.*⁴⁷ calculated $a_{ep} = 21$ meV for bulk-like ZB CdSe epilayers. This shows that the increased confinement in the NPLs has reduced the average exciton–phonon coupling, which is also evident from the significant reduction in average phonon temperature of 305 K in bulk ZB CdSe.²¹

Moreover, the exciton–phonon interaction induced intraband scattering causes transition energy broadening. The temperature dependence of the linewidth of excitonic peaks is given by^{26,48}

$$\Gamma(T) = \Gamma_0 + \gamma_{AC}T + \frac{\Gamma_{LO}}{e^{(\hbar\omega_{LO}/k_B T)} - 1} \quad (11)$$

where Γ_0 is the inhomogeneous broadening due to intrinsic effects (*e.g.* alloy disorder, impurities). γ_{AC} accounts for the exciton–acoustical phonon interaction. The last term comes from exciton–longitudinal optical (LO) phonon Fröhlich interaction. For practical purposes, the contribution of γ_{AC} compared with Γ_{LO} is negligible, hence sometimes it is considered zero.^{10,49} At cryogenic range, particularly <50 K, the linewidth gradient drastically decreases.^{10,32} therefore extrapolating our data of $\geq RT$ to lower temperatures would underestimate Γ_0 . We have used $\Gamma_0 = 32.5$ meV from ref. 10 following their linear fit at a low temperature range of 10–50 K. Further, based on the Raman spectra measurements of CdSe NPLs¹⁰ and QDs,¹² we have taken $\hbar\omega_{LO} = 25$ meV, to fit the other parameters of eqn (11) using the ascending temperature data from Fig. 8b. We found $\Gamma_{LO} = 236.3 \pm 11.8$ meV and $\gamma_{AC} = 0.38 \pm 0.03$ meV, suggesting that the LO phonon contribution is much larger compared with that of the acoustic phonon, consistent with the calculations of Rudin *et al.*⁴⁸ Compared with bulk-like CdSe epilayers ($\gamma_{AC} = 0.084$ meV),⁴⁷ NPLs have much higher γ_{AC} due to an increase in acoustic phonon coupling caused by a reduced dimensionality of the system, which is theoretically consistent.⁵⁰ The interaction between excitons and LO phonons is dictated by the Fröhlich interaction, which is coulombic in nature and caused by the longitudinal electric field produced by LO phonons. Therefore, $\hbar\omega_{LO}$ and Γ_{LO} are related in the sense that a larger $\hbar\omega_{LO}$ induces a stronger Fröhlich interaction and a larger Γ_{LO} . Valerini *et al.*⁵¹ have shown the presence of multiple temperature-dependent non-radiative pro-

cesses in PL relaxation dynamics. At higher temperatures, the contribution of LO phonons becomes predominant, eventually dominating the excitonic linewidth.⁴⁹

Furthermore, with increasing temperature, we also have a substantial reduction in the PL intensity as the excitons are trapped in the nonradiative centers, likely at NPL surfaces and dissociate into the continuum states. The integrated intensity of the PL spectra with varying temperatures is given by^{47,52}

$$I(T) = I(0)/[1 + C \cdot e^{-E_a/k_B T}] \quad (12)$$

where $I(0)$ and $I(T)$ are the integrated PL intensities at 0 K and T K, respectively. The fitting constant C is related to the radiative and nonradiative lifetimes and E_a is the activation energy of the nonradiative channel. We fit the ascending temperature data of Fig. 8c with eqn (12) to obtain $E_a = 494 \pm 6$ meV. Heating above RT induces both reversible and irreversible losses in intensity, and the latter restricts it to trace back upon cooling⁵³ (see Fig. 8d). Irreversible losses are generally caused by chemical processes like ligand loss or oxidative degradation damaging the NPL surface which disturbs the repopulation of mobile holes and electrons.⁵⁴ The extent to which the PL intensity is retraced in Fig. 7b is due to reversible losses caused by dynamic and static quenching.⁵³ Upon heating, dynamic quenching activates the thermally activated non-radiative recombination paths compared with radiative paths while static quenching causes the ratio of dark to bright particles to increase, inducing non-radiative decay. While actively heating up to 90 °C took us a few minutes, every successive 10 °C fall took an increasingly longer time – 2, 4, 6, 11, 19 and 32 minutes till 30 °C and even longer to RT. The Newton's cooling constant following $T(t) = T_a + \Delta T_0 e^{-kt}$ yields $k = 0.089 \text{ min}^{-1}$. An attempt to fit the descending T integrated intensity with eqn (12) yields a poor chi-square fit, as expected, since the irreversible losses incurred over a span of almost 1 h disturbs the liable excitonic properties. If the cooling is conducted in a vacuum environment (to avoid losses due to oxidation), it will result in an improved intensity recovery.

3.3 Comparison of theoretical and experimental results

In sections 3.1 and 3.2, we have studied the temperature-dependent optoelectronic properties of CdSe NPLs from a theoretical and experimental point of view. Here we combine and compare our findings, and simulate the PL spectra for varying temperatures, as shown in Fig. 9. A PL spectrum is characterized by three main parameters:

- PL peak position: We have theoretically calculated the temperature-dependent E1–H1 transition energy values (Fig. 1a), using the 8-band $k\cdot p$ method described in section 2.1 and the material parameters from Table 1. The Hamiltonian matrix was solved by direct diagonalization to obtain the electronic structure and eigenenergy values, and E1–H1 transition energy (equivalent of the PL peak position). It matches excellently with the experimental data of the PL peak position, as shown in Fig. 8a.

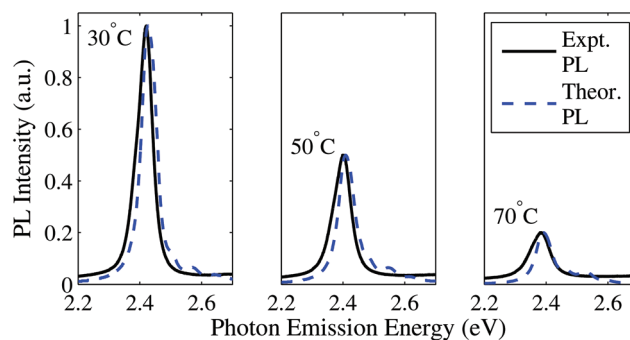


Fig. 9 Comparison of experimental (solid black) vs. theoretical (dotted blue) PL spectra of 4 ML CdSe NPLs at 30, 50 and 70 °C.

- PL linewidth: The PL spectrum undergoes spectral broadening due to several empirical factors, such as local and extended structural defects, size dispersion, alloy disorders and impurities, which affects its linewidth.³¹ Thus, different 4 ML CdSe NPL samples may have varying linewidths at the same temperature. We have used the experimental linewidth data of ascending temperature to extract the intraband relaxation time ($\tau_{in} = 2\hbar/\text{FWHM}$) used in our simulation as described in the calculation of the spontaneous radiative rate from the excitonic bound states and continuum-states in section 2.2. This helps to model the linewidth of the simulated PL spectra according to the Lorentzian broadening lineshape [eqn (9)] for an accurate estimate. The extracted τ_{in} is shown in Fig. 8b.

- PL intensity: We have calculated the relative PL intensity, which shows an exponential fall with temperature, as verified experimentally. However, the experimental PL intensity (arbitrary units) is not the absolute total emission. It is therefore of interest to study and compare the relative intensity variation with temperature, which is influenced by several parameters such as Fermi factor, TME, *etc.* [see eqn (7) and (8)]. Our theoretically predicted relative PL intensities have a very good comparison with the experimental intensities of ascending temperature, as shown in Fig. 8c.

The database of theoretical and experimental (ascending and descending temperature) results is given in the ESI.† Employing the above mentioned approach, we have studied the PL spectra of the 4 ML CdSe NPLs at varying temperatures. Fig. 9 shows a comparison between the experimental and theoretically calculated PL spectra at 30 °C, 50 °C and 70 °C. For a clear comparison of peak positions, linewidths and intensities, we have normalized both the experimental and theoretical PL spectra with respect to the PL peak at RT. The experimental and theoretical PL spectra match appreciably, which is consistent with the results presented in Fig. 8. In the ESI,† we have compared, extended and validated our calculations and measurements with the existing low temperature results from the literature. We have studied the temperature-dependent PL peak positions (E1–H1 transition energies), PL linewidth and relative PL intensity in tandem with the results

from the seminal works of Achtstein *et al.*¹⁰ and Erdem *et al.*⁴⁵ to validate our results.

4 Summary and conclusion

In summary, we have comprehensively studied the electronic bandstructure, probability of band mixing, charge densities, optical transition matrix element, characteristic PL emission energy, linewidth and integrated intensity of CdSe NPLs – as a function of temperature, which is of critical importance particularly for commercial device applications at elevated temperatures. Our theoretical investigations are based on a framework that relies on the effective-mass envelope function theory and density-matrix theory. From the quantum physics and optoelectronics point of view, the implications of a rise in the operation temperature of NPLs are many-fold, such as (i) a reduction in effective band-edge transition energy, (ii) a fall in optical transition matrix element strength, (iii) a reduction in intraband state gaps, faster so in CB compared with VB, (iv) a promotion of interband e–h coupling, (v) a modification in *hh–lh–so* band mixing probabilities, (vi) a reduction in Fermi factor, (vii) a shift of CB and VB quasi Fermi energy levels towards the band edges, and reduction in quasi Fermi separation, (viii) an invariance in the charge density profile, (ix) a redshift in peak photon emission energy in PL spectra, (x) a widening of PL spectral linewidth owing to intraband scattering, (xi) an exponential fall in PL integrated intensity, and (xii) a phenomenological evidence of reversible and irreversible losses induced, which affects sample quality and dictates PL traceability.

In conclusion, we have theoretically and experimentally studied the temperature-dependent optoelectronic characteristics of quasi-2D colloidal CdSe NPLs and established a model to predict and study the electronic bandstructure and PL spectra of NPLs at any arbitrary temperature, which can be effectively used by experimentalists to optimize device design iterations.

5. Experimental methods

5.1 Synthesis techniques

We have synthesized 4 ML colloidal CdSe NPLs using a synthesis protocol similar to those used in ref. 38 and 40–42. The following chemicals were used: cadmium acetate dihydrate $\text{Cd}(\text{OAc})_2 \cdot 2\text{H}_2\text{O}$, oleic acid, technical grade 1-octadecene, cadmium nitrate, cadmium nitrate, *n*-hexane, powder form selenium and myristic acid sodium salt. These were procured from Sigma Aldrich. The first step is to synthesize cadmium (myristate)₂ by dissolving 1.23 g of cadmium nitrate in methanol (40 mL). This was followed by dissolving sodium myristate (3.13 g) in methanol (250 mL) for 60 min with continuous stirring. When the two solutions were mixed, a white precipitate was formed after full dissolution. This precipitate was washed with methanol and dried under vacuum for about 24 h. 12 mg

(0.15 mmol) of selenium (Se) and 170 mg (0.3 nmol) of Cd (myristate)₂ were introduced in a three-neck flask along with 15 mL of octadecene (ODE) and degassed under vacuum. Under an argon (Ar) flow, the mixture was heated up to 240 °C, and maintained at it for 10 min. When the color of the solution became yellowish, at ~195 °C, 80 mg (0.30 mmol) of $\text{Cd}(\text{OAc})_2 \cdot 2\text{H}_2\text{O}$ was introduced. 5 mL of *n*-hexane and 0.5 mL of oleic acid were added at the end of the synthesis, and the solution was allowed to cool down to RT. A centrifuge was used to precipitate the NPLs before storing them in hexane. This synthesis also produces some 5 ML NPLs and spherical nanocrystals with distinctly different emission wavelengths. The 4 ML NPLs were separated from the rest using selective precipitation.

5.2 Purification and film preparation

The synthesized NPLs were centrifuged for 5 min at 4500 rpm, followed by removal of the supernatant solution. Nitrogen was used to dry the precipitate, before dissolving it in hexane for centrifugation for 10 min at 4500 rpm. The supernatant solution was made turbid by addition of ethanol, followed by centrifuging again for 10 min at 4500 rpm. Finally, using a 0.20 μm filter, the dissolved precipitate in hexane was filtered. Later, piranha solution was used for 30 min to clean quartz substrates of 1.5 × 1.5 cm size followed by DI-water. This was dried at 80 °C for 30 min in an oven and the filtered solution was spin-coated for 1 min at 2000 rpm to prepare solid thin-films of NPLs.

5.3 TEM and optical characterization

High-resolution transmission electron microscopy (TEM) images of NPL samples were taken on a JEOL JEM-2010 HR TEM operating at 200 kV, which has a resolution of ~0.22 nm. Steady state PL spectra measurements were done using a cooled iDus CCD system. The time resolved PL measurements were done with a Becker & Hickl DCS 120 confocal scanning FLIM system with an excitation laser of 375 nm. The system has temporal resolution of 200 ps.

Acknowledgements

We would like to acknowledge: NTU start-up grant, MOE AcRF Tier 1 grant RG 70/15 & RG 182/14, NRF-RF-2009-09, NRF-CRP-6-2010-02, A*STAR, ESF-EURYI and TUBA-GEBIP.

References

- 1 S. Ithurria and B. Dubertret, *J. Am. Chem. Soc.*, 2008, **130**, 16504.
- 2 B. GuzelTURK, Y. Kelestemur, M. Olutas, S. Delikanli and H. V. Demir, *ACS Nano*, 2014, **8**, 6599.
- 3 Z. Chen, B. Nadal, B. Mahler, H. Aubin and B. Dubertret, *Adv. Funct. Mater.*, 2014, **24**, 295–302.

- 4 S. Ithurria, M. D. Tessier, B. Mahler, R. P. Lobo, B. Dubertret and A. L. Efros, *Nat. Mater.*, 2011, **10**, 936.
- 5 R. Benchamekh, N. A. Gippius, J. Even, M. O. Nestoklon, J. M. Jancu, S. Ithurria, B. Dubertret, A. L. Efros and P. Voisin, *Phys. Rev. B: Condens. Matter*, 2014, **89**, 035307.
- 6 M. D. Tessier, B. Mahler, B. Nadal, H. Heuclin, S. Pedetti and B. Dubertret, *Nano Lett.*, 2013, **13**, 3321.
- 7 B. Guzelturk, M. Olutas, S. Delikanli, Y. Kelestemur, O. Erdem and H. V. Demir, *Nanoscale*, 2015, **7**, 2545.
- 8 J. Q. Grim, S. Christodoulou, F. Di Stasio, R. Krahne, R. Cingolani, L. Manna and I. Moreels, *Nat. Nanotechnol.*, 2014, **9**, 891.
- 9 Y. Zhao, C. Riemersma, F. Pietra, R. Koole, C. de Mello Donegá and A. Meijerink, *ACS Nano*, 2012, **6**, 9058–9067.
- 10 A. W. Achtstein, A. Schliwa, A. Prudnikau, M. Hardzei, M. V. Artemyev, C. Thomsen and U. Woggon, *Nano Lett.*, 2012, **12**, 3151.
- 11 C. Ji, Y. Zhang, T. Zhang, W. Liu, X. Zhang, H. Shen, Y. Wang, W. Gao, Y. Wang, J. Zhao and W. W. Yu, *J. Phys. Chem. C*, 2015, **119**, 13841–13846.
- 12 P. Jing, J. Zheng, M. Ikezawa, X. Liu, S. Lv, X. Kong, J. Zhao and Y. Masumoto, *J. Phys. Chem. C*, 2009, **113**, 13545–13550.
- 13 Q. Le-Van, X. Le Roux, T. V. Teperik, B. Habert, F. Marquier, J.-J. Greffet and A. Degiron, *Phys. Rev. B: Condens. Matter*, 2015, **91**, 085412.
- 14 J. Chen, W. J. Fan, Q. Xu, X. W. Zhang, S. S. Li and J. B. Xia, *J. Appl. Phys.*, 2009, **105**, 123705.
- 15 Z.-G. Song, S. Bose, W.-J. Fan and S.-S. Li, *J. Appl. Phys.*, 2016, **119**, 143103.
- 16 S. Bose, W. J. Fan, J. Chen, D. H. Zhang and C. S. Tan, 12th International Conference on Fiber Optics and Photonics, 2014, p. S4D.5.
- 17 S. Bose, W. Fan, C. Jian, D. Zhang and C. Tan, Silicon-Germanium Technology and Device Meeting (ISTDM), 2014 7th International, 2014, pp. 129–130.
- 18 S. Bose, Z. Song, W. J. Fan and D. H. Zhang, *J. Appl. Phys.*, 2016, **119**, 143107.
- 19 W. Shan, J. J. Song, H. Luo and J. K. Furdyna, *Phys. Rev. B: Condens. Matter*, 1994, **50**, 8012.
- 20 S. Z. Karazhanov and L. L. Y. Voon, *Semiconductors*, 2005, **39**, 161.
- 21 O. Madelung, *Semiconductors: Data Handbook*, Springer, 2004.
- 22 V. Kumar, *J. Phys. Chem. Solids*, 2000, **61**, 91–94.
- 23 M. L. Landry, T. E. Morrell, T. K. Karagounis, C.-H. Hsia and C.-Y. Wang, *J. Chem. Educ.*, 2014, **91**, 274–279.
- 24 J. Micallef, E. Li and B. L. Weiss, *Superlattices Microstruct.*, 1993, **13**, 315.
- 25 E. H. Li and B. L. Weiss, *Proc. SPIE*, 1992, **1675**, 98–108.
- 26 S. L. Chuang, *Physics of Photonic Devices*, Wiley, 2009.
- 27 J. Piprek, *Semiconductor Optoelectronic Device*, Academic Press, Boston, ch. 5, 2003, pp. 121–139.
- 28 M. Sugawara, *Self-Assembled InGaAs/GaAs Quantum Dots*, Elsevier, 1999, vol. 60, pp. 1–116.
- 29 W. J. Fan, M. F. Li, T. C. Chong and J. B. Xia, *J. Appl. Phys.*, 1996, **80**, 3471.
- 30 Y. P. Varshni, *Physica*, 1967, **34**, 149–154.
- 31 I. H. Calderon, *II-VI Semiconductor Materials and their Applications*, Taylor and Francis, New York, 2002, vol. 12.
- 32 S. Logothetidis, M. Cardona, P. Lautenschlager and M. Garriga, *Phys. Rev. B: Condens. Matter*, 1986, **34**, 2458–2469.
- 33 L. I. Burov, E. V. Lebedok, V. K. Kononenko, A. G. Ryabtsev and G. I. Ryabtsev, *J. Appl. Spectrosc.*, 2007, **74**, 878–883.
- 34 S.-H. Wei and A. Zunger, *Phys. Rev. B: Condens. Matter*, 1988, **37**, 8958–8981.
- 35 M. Olutas, B. Guzelturk, Y. Kelestemur, K. Gungor and H. V. Demir, *Adv. Funct. Mater.*, 2016, **26**, 2891–2899.
- 36 G. H. V. Bertrand, A. Polovitsyn, S. Christodoulou, A. H. Khan and I. Moreels, *Chem. Commun.*, 2016, **52**, 11975–11978.
- 37 A. W. Achtstein, A. Antanovich, A. Prudnikau, R. Scott, U. Woggon and M. Artemyev, *J. Phys. Chem. C*, 2015, **119**, 20156–20161.
- 38 M. D. Tessier, P. Spinicelli, D. Dupont, G. Patriarche, S. Ithurria and B. Dubertret, *Nano Lett.*, 2014, **14**, 207–213.
- 39 B. Mahler, B. Nadal, C. Bouet, G. Patriarche and B. Dubertret, *J. Am. Chem. Soc.*, 2012, **134**, 18591–18598.
- 40 Y. Kelestemur, B. Guzelturk, O. Erdem, M. Olutas, K. Gungor and H. V. Demir, *Adv. Funct. Mater.*, 2016, **26**, 3570–3579.
- 41 M. Olutas, B. Guzelturk, Y. Kelestemur, A. Yeltik, S. Delikanli and H. V. Demir, *ACS Nano*, 2015, **9**, 5041–5050.
- 42 B. Guzelturk, O. Erdem, M. Olutas, Y. Kelestemur and H. V. Demir, *ACS Nano*, 2014, **8**, 12524–12533.
- 43 E. M. Hutter, E. Bladt, B. Goris, F. Pietra, J. C. van der Bok, M. P. Boneschanscher, C. de, M. Donegá, S. Bals and D. Vanmaekelbergh, *Nano Lett.*, 2014, **14**, 6257–6262.
- 44 J. R. Lakowicz, *Principles of Fluorescence Spectroscopy*, Springer, Boston, USA, 2006.
- 45 O. Erdem, M. Olutas, B. Guzelturk, Y. Kelestemur and H. V. Demir, *J. Phys. Chem. Lett.*, 2016, **7**, 548–554.
- 46 O. Halder, A. Pradhani, P. K. Sahoo, B. Satpati and S. Rath, *Appl. Phys. Lett.*, 2014, **104**, 182109.
- 47 C. Chia, C. Yuan, J. Ku, S. Yang, W. Chou, J. Juang, S. Hsieh, K. Chiu, J. Hsu and S. Jeng, *J. Lumin.*, 2008, **128**, 123–128.
- 48 S. Rudin, T. L. Reinecke and B. Segall, *Phys. Rev. B: Condens. Matter*, 1990, **42**, 11218–11231.
- 49 G. Perna, V. Capozzi and M. Ambrico, *J. Appl. Phys.*, 1998, **83**, 3337–3344.
- 50 T. Takagahara, *Phys. Rev. Lett.*, 1993, **71**, 3577–3580.
- 51 D. Valerini, A. Cretí, M. Lomascolo, L. Manna, R. Cingolani and M. Anni, *Phys. Rev. B: Condens. Matter*, 2005, **71**, 235409.
- 52 M. Leroux, N. Grandjean, B. Beaumont, G. Nataf, F. Semond, J. Massies and P. Gibart, *J. Appl. Phys.*, 1999, **86**, 3721–3728.
- 53 X. Cai, J. E. Martin, L. E. Shea-Rohwer, K. Gong and D. F. Kelley, *J. Phys. Chem. C*, 2013, **117**, 7902–7913.
- 54 T.-C. Liu, Z.-L. Huang, H.-Q. Wang, J.-H. Wang, X.-Q. Li, Y.-D. Zhao and Q.-M. Luo, *Anal. Chim. Acta*, 2006, **559**, 120–123.